



## Microstructural, mechanical, and tribological characterization of Hybrid Si<sub>3</sub>N<sub>4</sub>–BN nanoparticle-reinforced AA5052 surface composites fabricated by multi-pass friction stir processing

Rajamuthukumar Karrupusamy Subbian<sup>1</sup> , Sasikumar Ayyanar<sup>1</sup>, Sankarapandian Sankarasabapathi<sup>2</sup>,  
Santhosh Velmurugan<sup>3</sup> 

<sup>1</sup>Government College of Technology, Coimbatore, Tamil Nadu, India.

<sup>2</sup>Alagappa Chettiar Government College of Engineering and Technology, Karaikudi, Tamil Nadu, India.

<sup>3</sup>Karpagam Academy of Higher Education, Coimbatore, Tamil Nadu, India.

e-mail: rmk161978@gmail.com, sasikumar@gmail.com, sankarsaba@yahoo.com, santhoshshivan.v@gmail.com

### ABSTRACT

This study investigated the improved surface properties of a hybrid material containing silicon nitride (Si<sub>3</sub>N<sub>4</sub>) and boron nitride (BN) nanoparticles introduced via a three-stage friction stir processing (FSP) method. Unlike the traditional blind hole powder addition method, which results in particle aggregation, the longitudinal groove method achieves a more uniform distribution of reinforcements. Three Si<sub>3</sub>N<sub>4</sub>:BN mixture ratios (70:30, 60:40, and 50:50) were prepared, and their effects on microstructural changes, mechanical response, and tribological properties were systematically analyzed. Compared to the untreated alloy, the 60:40 composition provided the most balanced properties, with a 42% increase in microhardness (121.1 HV), a 58% reduction in wear rate ( $1.99 \times 10^{-4} \text{ mm}^3/\text{N}^4\text{m}$ ), and a low coefficient of friction of 0.29. The 70:30 formulation exhibited the highest tensile strength (131.96 MPa), an 18% increase. Microstructural observations confirmed the formation of refined equiaxed grains (approximately 5.2  $\mu\text{m}$ ) and uniformly dispersed nanoparticles due to dynamic recrystallization and Zener pinning. Phase analysis using X-ray diffraction (XRD) and EDS confirmed stable  $\alpha$ -Al, Si<sub>3</sub>N<sub>4</sub>, and h-BN phases, with no intermetallic compounds. These results demonstrate that multi-pass FSP with hybrid ceramic reinforcement can effectively improve the surface integrity of aluminum alloys and lay the foundation for future research into corrosion resistance, high-temperature stability, and fatigue performance in aerospace, marine, and automotive applications.

**Keywords:** AA5052 alloy; Friction stir processing; Silicon nitride; Boron nitride; Tribological properties.

### 1. INTRODUCTION

In recent years, metal-ceramic composites have attracted widespread attention in the field of advanced engineering due to their dual role in improving the structural integrity and enhancing the functional properties of metallic materials. These composites are particularly attractive due to their high strength-to-weight ratio, thermal stability, stiffness, and durability, making them promising materials for aerospace, automotive, defense, and marine applications, where reliability is crucial [1, 2]. Among various composite systems, metal matrix composites (MMCs) have attracted much attention due to their superior mechanical properties, wear resistance, and flexibility in controlling thermal expansion behavior compared to traditional single-metal alloys [3, 4]. Aluminum and its alloys are widely used as the matrix of such composites due to their low density, corrosion resistance, recyclability, and excellent formability. Among these alloys, AA5052 alloy is commonly used in marine structures, automotive body panels, and transportation components due to its excellent weldability and corrosion resistance in saltwater conditions [5, 6]. However, due to its relatively low hardness and poor tribological properties, AA5052 is not suitable for manufacturing components exposed to friction, sliding, or abrasive environments [7]. To alleviate these shortcomings, researchers have reinforced aluminum alloys with ceramic phases such as Al<sub>2</sub>O<sub>3</sub>, SiC, TiC, Si<sub>3</sub>N<sub>4</sub>, and BN to improve their hardness, wear resistance, and load-bearing capacity [8, 9, 10].

Friction stir processing (FSP), an adaptation of friction stir welding, has emerged as a versatile solid-state technique for fabricating aluminum matrix composites (AMCs). Unlike melt-based processing routes,

FSP minimizes porosity and segregation while promoting uniform particle dispersion and grain refinement through intense plastic deformation and dynamic recrystallization [11, 12, 13]. Different strategies have been employed to introduce reinforcements, ranging from simple groove filling to blind-hole powder insertion. For instance, Nabi *et al.* [14] successfully incorporated NiTi particles in AA5052 using longitudinal grooves, while Qu *et al.* [15] employed spiral and rectangular grooves to embed  $\text{Al}_2\text{O}_3$  and SiC in AA6061. In contrast, Mehta and Vishvesh [16] adopted a blind-hole filling method for  $\text{B}_4\text{C}$ -reinforced AA6061 and achieved significant improvements in wear resistance. However, blind-hole methods often introduce non-uniform particle distribution and increase the risk of agglomeration, whereas groove-based filling ensures a more continuous and homogeneous dispersion of powders during FSP, particularly under multi-pass conditions.

The performance of FSP-fabricated composites is strongly influenced by tool geometry and processing parameters such as rotation speed, traverse rate, tilt angle, and axial load. Optimized processing conditions promote sufficient heat input and plastic flow, which in turn refine grain structures and strengthen particle–matrix bonding. Studies such as those by Vignesh *et al.* [17] and Yadav *et al.* [18] demonstrated that careful control of parameters improves hardness and wear resistance, while Girish and Anandakrishnan [19] highlighted the effectiveness of statistical methods, including Taguchi design, for systematic optimization. More recently, the role of nanoscale reinforcements has been investigated, showing that additions of  $\text{ZrO}_2$ ,  $\text{TiB}_2$ , and WC can produce ultrafine grains and enhance both mechanical strength and wear resistance in aluminum and magnesium alloys [20, 21, 22].

Beyond single-phase reinforcement, hybrid strategies are increasingly emphasized for exploiting the complementary benefits of different ceramic systems. For example,  $\text{Si}_3\text{N}_4$  offers high hardness, fracture toughness, and thermal stability, making it a strong load-bearing reinforcement [23]. Conversely, hexagonal BN provides intrinsic lubricity and chemical inertness, enabling reduced friction and improved wear performance [24]. Previous studies have explored hybrid composites using powder metallurgy [25], melt casting [26], and laser-based approaches, yet very few reports exist on their integration into AA5052 surfaces using multi-pass FSP. Recent investigations, including those by Kumar *et al.* [27], Zhao *et al.* [28], and Singh *et al.* [29], have underscored the importance of combining hard and lubricating reinforcements to simultaneously enhance strength and tribological performance, but such studies remain largely limited to AA6061 and AA7075 alloys [30].

Despite these advancements, three key research gaps remain. First, FSP investigations on AA5052 have largely focused on single reinforcements, leaving insufficient understanding of how hybrid nanoparticles behave in this specific alloy. Second, systematic comparisons between reinforcement distribution achieved through multi-pass groove filling and blind-hole techniques are scarce, and the relative merits of each method are not fully established. Third, very few works have evaluated the combined influence of hybrid reinforcements on microstructural refinement, tensile behavior, wear resistance, and fracture mechanisms under realistic service conditions [31, 32, 33, 34].

To address this issue, this study used a three-stage FSP process to prepare AA5052 surface composites reinforced with  $\text{Si}_3\text{N}_4$ -BN hybrid nanoparticles. Three weight ratios (70:30, 60:40, and 50:50) were used to evaluate the effects of the hybrid components on microstructure, phase stability, hardness, tensile strength, and tribological properties. The results of this study demonstrated the feasibility of combining load-bearing ( $\text{Si}_3\text{N}_4$ ) and self-lubricating (BN) reinforcements to develop surface composites with a balance of strength and wear resistance. This study also lays the foundation for future research on corrosion resistance in marine environments, high-temperature stability in aerospace applications, and fatigue resistance under cyclic loading, expanding the applicability of AA5052-based composites in critical engineering environments.

## 2. MATERIALS AND METHODS

### 2.1. Materials

Commercial aluminum alloy AA5052 sheets (100 mm × 50 mm × 6 mm) were purchased from Coimbatore Metal Mart, India, and used as the substrate. This alloy was selected for its excellent corrosion resistance, weldability, and wide suitability for use in marine and structural environments, but its limited wear resistance makes it an ideal candidate for ceramic reinforcement. Its chemical composition is listed in Table 1, and its basic mechanical properties are summarized in Table 2. The hybrid ceramic reinforcement, consisting of silicon nitride ( $\text{Si}_3\text{N}_4$ ) and boron nitride (BN) nanopowders (average particle size 100–200 nm, 99% purity), was purchased from Ultra Nanotech Pvt. Ltd., India. Prior to mixing, the powders were premixed in three weight ratios (70:30, 60:40, and 50:50), as shown in Table 3.

### 2.2. Groove preparation and powder filling

Each AA5052 sheet is milled with a central longitudinal groove (100 mm long, 1 mm wide, and 2 mm deep) using a CNC milling cutter. This structure, chosen over blind hole filling, facilitates continuous powder distribution

**Table 1:** Chemical composition of AA5052 alloy (wt%).

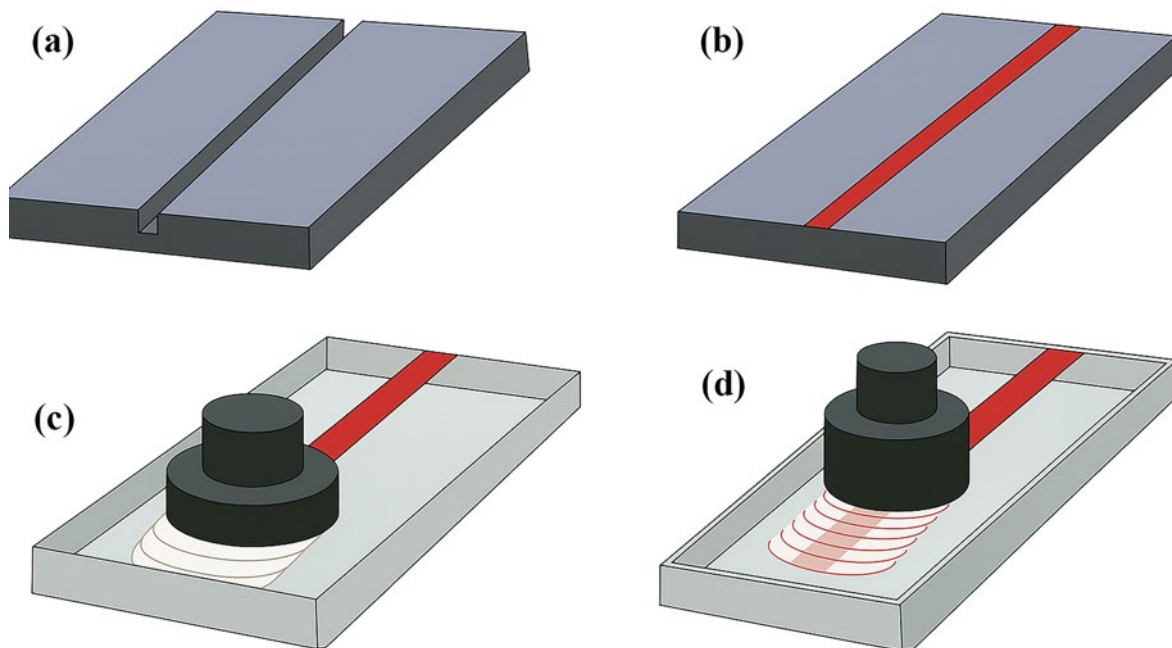
ELEMENT	Si	Fe	Cu	Mn	Mg	Cr	Zn	Al
Content	0.25	0.40	0.10	0.10	2.50	0.25	0.10	Balance

**Table 2:** Mechanical properties of AA5052 alloy.

PROPERTY	ULTIMATE TENSILE STRENGTH (MPa)	YIELD STRENGTH (MPa)	ELONGATION (%)	VICKERS HARDNESS (HV)	DENSITY (g/cm <sup>3</sup> )	MELTING POINT (°C)
Value	217	168	19.5	85	2.68	607

**Table 3:** Hybrid nanoparticle reinforcement compositions (wt%).

SAMPLE	Si <sub>3</sub> N <sub>4</sub> (%)	BN (%)
Sample 1	70	30
Sample 2	60	40
Sample 3	50	50


**Figure 1:** Schematic representation of the fabrication steps: (a) groove cutting, (b) reinforcement filling, (c) sealing with a pinless tool, and (d) multipass friction stir processing of AA5052 composites.

and minimizes the risk of agglomeration. After the groove is filled with a premixed nanoparticle mixture, a pinless tool path compresses and seals the powder, preventing material loss during subsequent processing. The overall manufacturing process is shown in Figure 1, and the groove before powder filling is shown in Figure 2.

### 2.3. Friction stir processing

FSP was performed using a modified vertical milling machine equipped with a non-consumable HHCCR steel tool, heat-treated to a hardness of approximately 60 HRC. The tool consisted of a threaded cylindrical pin (6 mm diameter, 2.5 mm length) and an 18 mm shoulder. The tool inclination angle and axial force were carefully adjusted to promote proper material flow and mixing.

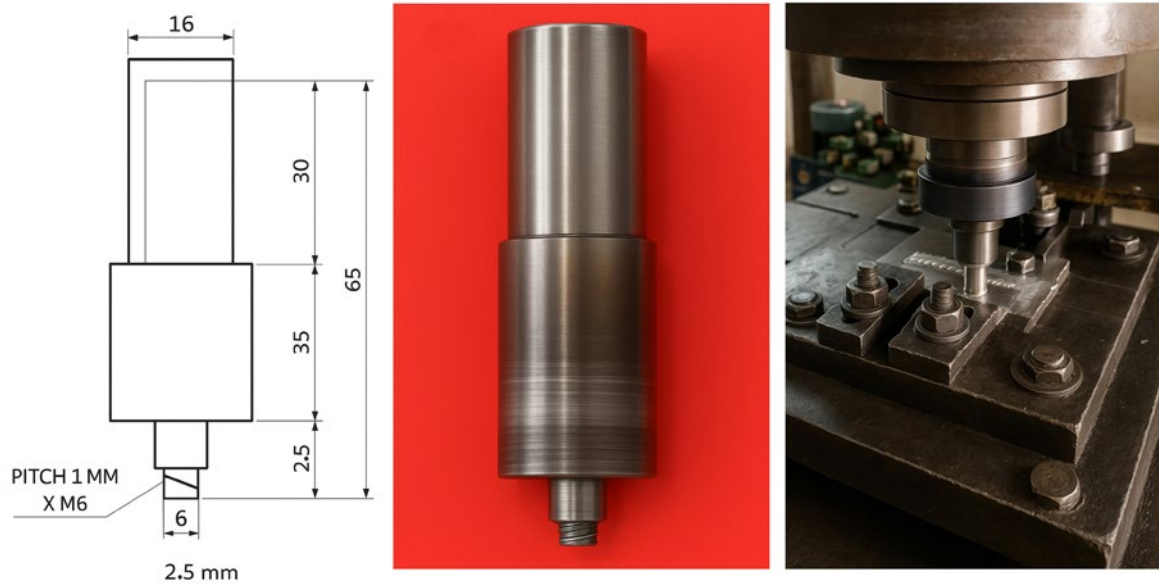


**Figure 2:** Photograph of the AA5052 plate with central longitudinal groove prior to powder filling, showing groove dimensions (length: 100 mm, width: 1 mm, depth: 2 mm).

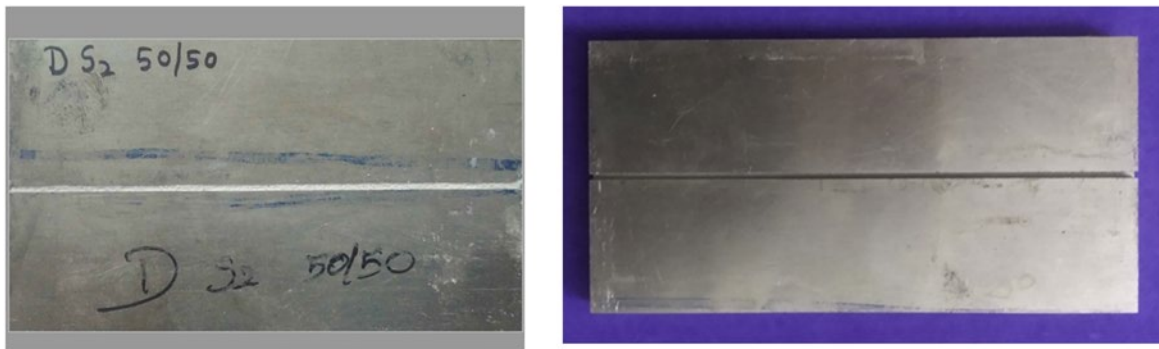


**Figure 3:** Photograph of the FSP tool and vertical milling machine setup used for processing, with labeled dimensions: threaded pin (6 mm diameter, 2.5 mm length) and tool shoulder (18 mm diameter).

**Table 4:** Friction stir processing parameters.

ROTATIONAL SPEED (rpm)	TRAVERSE SPEED (mm/min)	TOOL TILT ANGLE (°)	AXIAL FORCE (kN)	NUMBER OF PASSES	PIN DIAMETER (mm)	PIN LENGTH (mm)	SHOULDER DIAMETER (mm)
1000	25	1.2	6	3	6	2.5	18

To determine the most stable machining range while minimizing defects such as tunnel voids and particle aggregation, preliminary tests were conducted within a speed range of 800 to 1200 rpm and 20 to 35 mm/min. Based on these tests and literature recommendations, the optimized parameters used for all samples are listed in Table 4. Three nested passes were applied to improve uniformity. Representative photographs of the milling machine setup and tool assembly are shown in Figure 3.

#### 2.4. Sample sectioning and surface preparation

The treated plates were sliced and characterized perpendicular to the FSP direction, and after grinding (SiC 200–2000 grit), polishing with 0.5  $\mu\text{m}$  alumina, and observing the system using Keller reagent (2 mL HF + 3 mL HCl + 5 mL HNO<sub>3</sub> + 190 mL H<sub>2</sub>O) according to the standard metallurgical procedure (ASTM E3).



## 2.5. Microstructural and phase characterization

Preliminary microstructural observations were performed using an Olympus GX53 optical microscope. High-resolution imaging and particle scattering studies were performed using a Carl Zeiss Sigma 300 VP FESEM microscope (10–15 kV). Elemental distribution of the reinforcements was analyzed using EDS spectroscopy.

X-ray diffraction (XRD) was performed using a Bruker D8 Advance diffractometer using Cu K $\alpha$  radiation ( $\lambda = 1.5406 \text{ \AA}$ ) with a scan angle range of  $20^\circ$  to  $80^\circ$  ( $2\theta$ ) and a scan rate of  $2^\circ/\text{min}$ , in accordance with ASTM E1426. Before testing, the samples were ground to remove surface oxides. To complement the SEM/EDS analysis, multiple areas of the stir zone were analyzed, and grain size was measured using ImageJ software to confirm the homogeneity of the reinforcement. Representative FESEM micrographs and EDS results are presented in detail in Chapter 3.

## 2.6. Mechanical property evaluation

Vickers microhardness testing was conducted using a Mitutoyo HM-210B testing machine with a load of 100 gf and a hold time of 15 seconds (per ASTM E384). Indentations were made at 1 mm intervals along the center of the thickness, and the average of at least five measurements was obtained. Furthermore, hardness mapping was performed at multiple points in the stir zone to ensure uniform reinforcement distribution.

Small flat tensile specimens (per ASTM E8/E8M) were taken longitudinally from the stir zone and tested using a 100 kN FSA M-100 universal testing machine with a crosshead speed of 2 mm/min. Yield strength and elongation at 0.2% deflection were recorded. To ensure repeatability, at least three specimens were tested for each composition, and the corresponding stress-strain responses were analyzed for comparison.

## 2.7. Tribological testing

Dry wear tests were conducted using a Ducom TR-20LE pin-on-disc tribometer (ASTM G99). Cylindrical pins (10 mm  $\times$  6 mm) cut from the FSP region were pressed into a hardened EN31 steel disc (165 mm diameter) according to the parameters listed in Table 5. The wear track diameter was set to 100 mm. Mass loss was

**Table 5:** Pin-on-disc wear test parameters.

LOAD (N)	SLIDING SPEED (m/s)	SLIDING DISTANCE (m)	TRACK DIAMETER (mm)
15	1.2	750	100

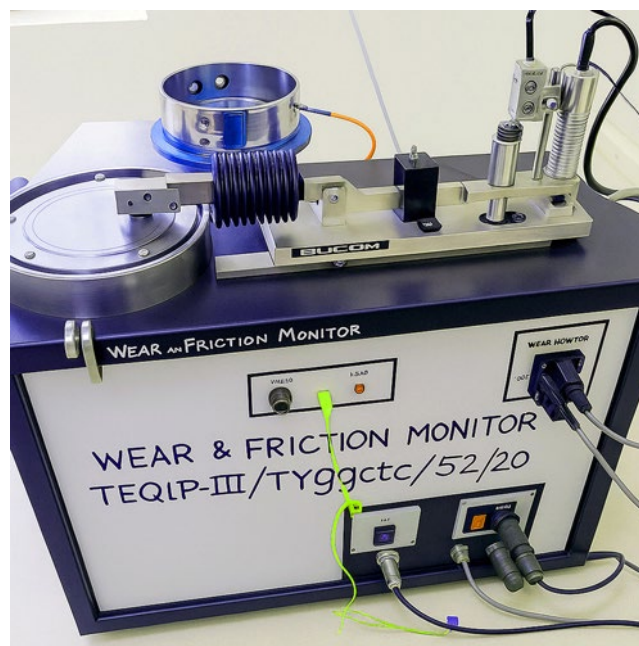


**Figure 4:** Photograph of the pin-on-disc tribometer (Ducom TR-20LE) used for dry sliding wear testing under ASTM G99 conditions.

measured using a Shimadzu AUW220D scale ( $\pm 0.01$  mg). The coefficient of friction was continuously monitored. After the test, the worn surfaces were analyzed using a scanning electron microscope (SEM) to determine the primary wear mechanism. The surface roughness (Ra) of the composites was measured using a Mitutoyo SJ-210 profilometer. A typical wear test setup is shown in Figure 4.

### 3. RESULTS AND DISCUSSION

#### 3.1. Reinforcement powder morphology

Before processing, the morphology of the reinforcing powder must be analyzed to determine its size and surface properties, which directly influence its reinforcing effect in the composite.  $\text{Si}_3\text{N}_4$  powder (Figure 5a) typically presents irregular polygonal particles with tilted particles and particle sizes ranging from 100 to 200 nanometers. At higher magnification (Figure 5b), these particles exhibit a rough and jagged surface, which facilitates a strong interfacial bond with the aluminum matrix during FSP. Meanwhile, BN particles are plate-like (Figure 5c), appearing as thin, lamellar flakes with a relatively smooth surface (Figure 5d). These morphologies suggest that they have complementary functions. The tilted  $\text{Si}_3\text{N}_4$  particles act as rigid, load-bearing reinforcements, enhancing strength and hardness, while the flat h-BN plates act as solid lubricants, reducing friction during sliding. Therefore, the combination of these two types of particles is expected to offer both reinforcement and tribological advantages in hybrid composites.

#### 3.2. Microstructure of FSP-fabricated composites

AA5052-based alloys typically exhibit elongated grains in cold-rolled material. After FSP treatment, the stir zone exhibits significant grain refinement and equiaxed morphology, resulting from dynamic recrystallization under intense plastic deformation and frictional heating. FESEM analysis (Figures 6a–c) reveals that reinforcements

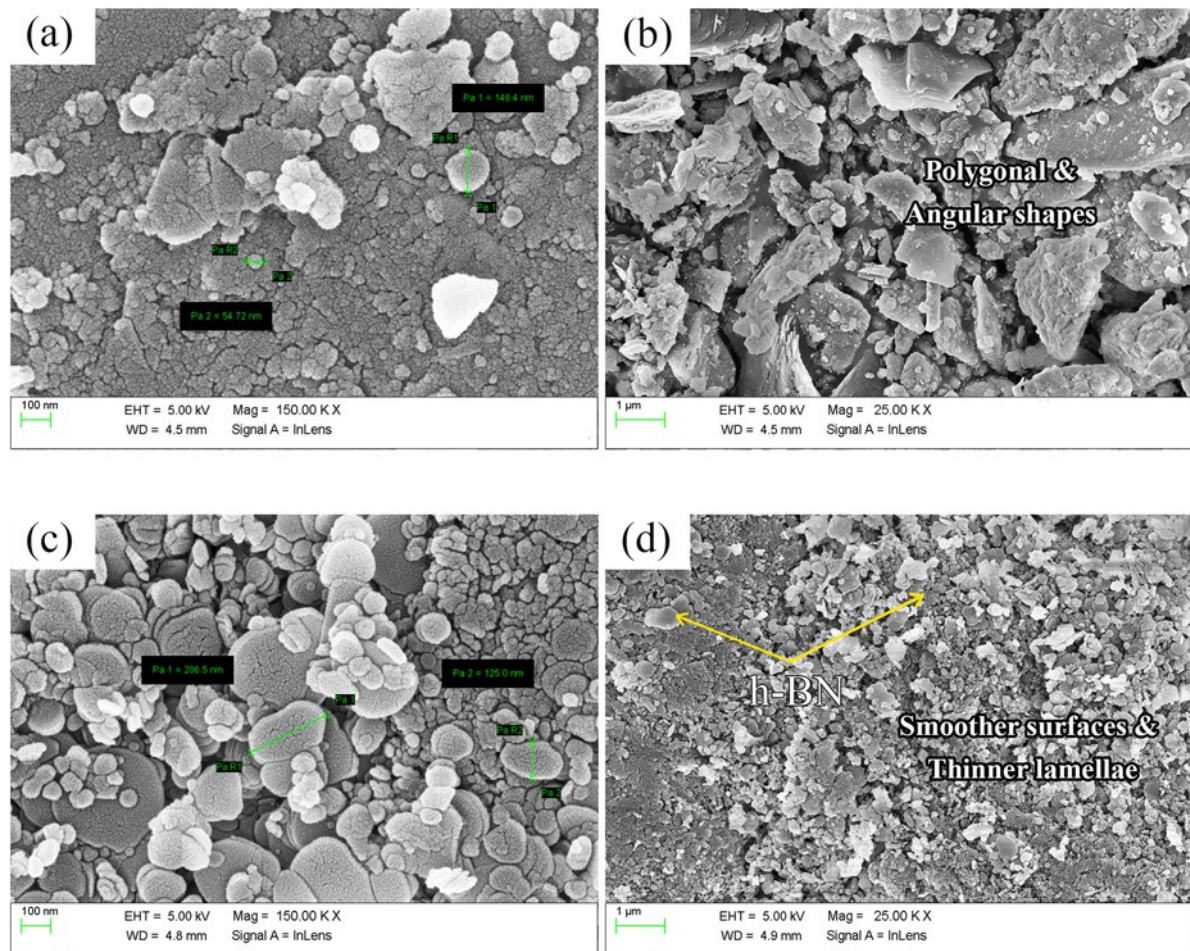


**Figure 5:** FESEM images of the reinforcement powders: (a, b)  $\text{Si}_3\text{N}_4$  particles with angular morphology and (c, d) flake-like BN particles with a layered structure.



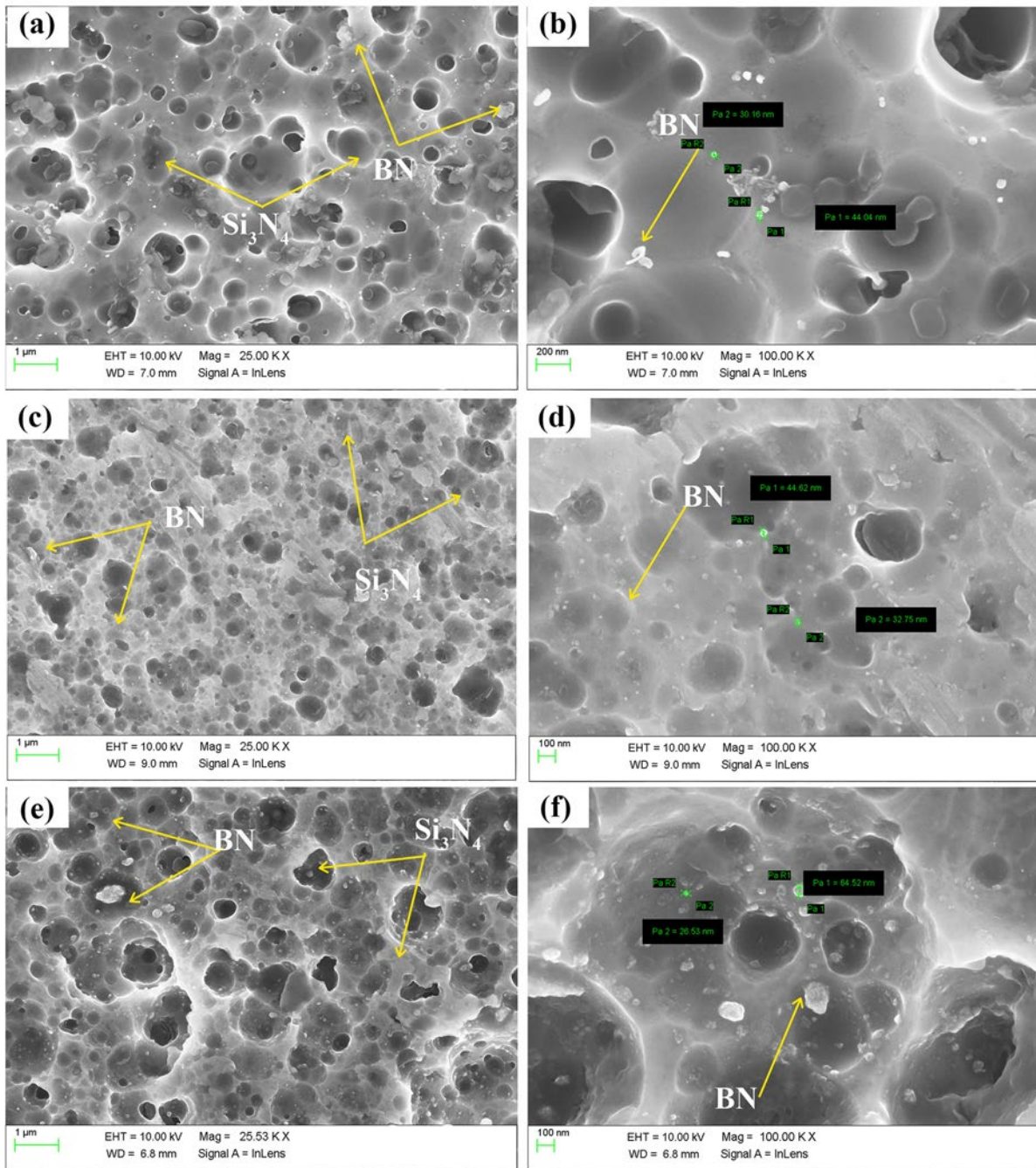


**Figure 6:** FESEM images of stir zones: (a, b) 70:30  $\text{Si}_3\text{N}_4$ -BN, (c, d) 60:40  $\text{Si}_3\text{N}_4$ -BN, and (e, f) 50:50  $\text{Si}_3\text{N}_4$ -BN composites.

of all compositions are uniformly distributed in the stir zone, without agglomeration or porosity. Among the three ratios, the  $\text{Si}_3\text{N}_4$ -BN 60:40 composite (Figure 6c) exhibits the most uniform nanoparticle dispersion and the smallest grain size after three repeated FSP stirring cycles. At higher magnifications (Figures 6d–f), BN platelets can be observed partially aligned along the cutting direction of the tool, while  $\text{Si}_3\text{N}_4$  remains randomly dispersed. The presence of reinforcements acts as nucleation sites for recrystallization, suppressing grain growth via the Zener pins and producing finer grains in the stir zone than those in the base alloy and the TMAZ. The disappearance of tunnel defects and pores further confirms that multi-pass FSP is effective in consolidating the hybrid reinforcement.

### 3.3. EDS elemental distribution

EDS spectroscopy, assessing the chemical distribution within the stir zone, confirmed the successful incorporation of the  $\text{Si}_3\text{N}_4$  and BN particles (Figures 7a–c). Strong signals for Si, B, N, Al, Mg, and Cr were observed

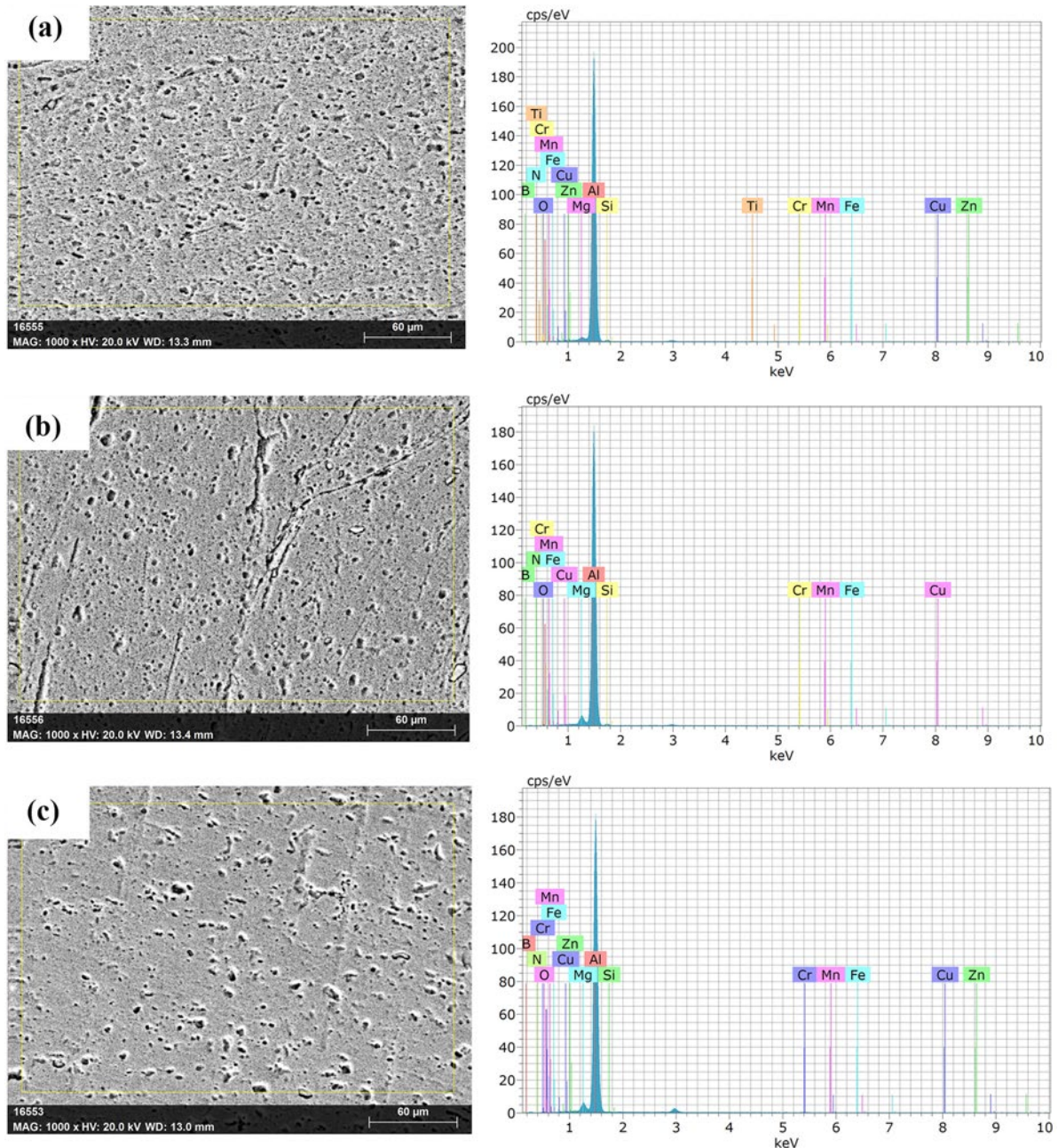


**Figure 7:** EDS spectra of the stir zone: (a) 70:30  $\text{Si}_3\text{N}_4$ -BN; (b) 60:40  $\text{Si}_3\text{N}_4$ -BN; (c) 50:50  $\text{Si}_3\text{N}_4$ -BN composites.

within the AA5052 matrix. The uniform intensity of reinforcement-related elements across the entire spectral region indicated a homogeneous particle distribution, consistent with microstructural observations. Importantly, no enriched regions or aggregates were detected, indicating that the three-stage FSP process effectively disintegrated agglomerates. Furthermore, elemental alignment with particle position indicated that the reinforcements were not dissolved into the matrix and remained intact during processing.

### 3.4. Phase analysis (XRD)

X-ray diffraction patterns from the stirred zone confirmed  $\alpha$ -Al as the primary matrix phase (Figure 8). Characteristic aluminum peaks were observed at  $2\theta \approx 38.4^\circ$ ,  $44.7^\circ$ ,  $65.1^\circ$ , and  $78.2^\circ$ , consistent with the FCC structure of the matrix alloy. Additional peaks corresponding to  $\text{Si}_3\text{N}_4$  and h-BN were also observed, confirming the maintenance of the reinforcement particles within the composite. Importantly, no peaks associated with secondary intermetallic compounds such as  $\text{AlN}$  or  $\text{AlB}_2$  were detected, indicating that the reinforcement remained chemically stable and did not react with the matrix. The lack of significant peak shifts or peak broadening indicates



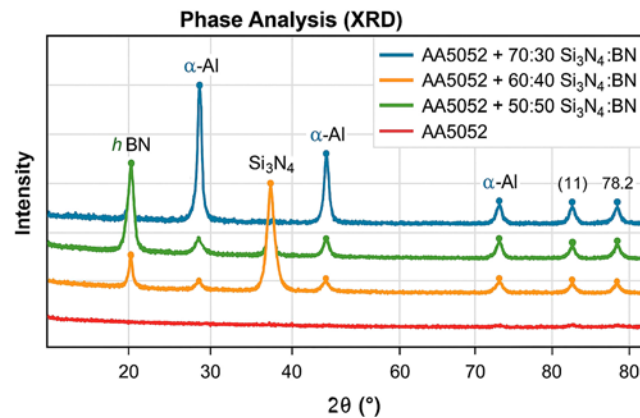


**Figure 8:** XRD patterns of AA5052 and hybrid composites showing peaks for  $\alpha$ -Al,  $\text{Si}_3\text{N}_4$ , and h-BN phases.

that the lattice integrity of the  $\alpha$ -Al was not disrupted by the addition of the nanoparticles. These results confirm that FSP provides physical addition of reinforcement rather than chemical alloying.

### 3.5. Microhardness behavior

The Microhardness evaluation revealed significant improvements in the stir zone of all reinforced composites compared to the unprocessed AA5052-based alloy (average hardness of approximately 85 HV). As shown in Figure 9, friction stir processing of nanoparticle hybrid reinforcements increased hardness from 113.6 to 121.1 HV, depending on the reinforcement ratio. The 60:40  $\text{Si}_3\text{N}_4$ -BN composite exhibited the highest hardness, approximately 121.1 HV, a 42% increase over the base alloy. The 50:50 and 70:30 composites exhibited slightly lower hardness, at 118.5 HV and 113.6 HV, respectively.

This significant increase in hardness is closely related to the microstructural changes induced during the multi-pass fusion pressure suppression (FSP) process. The combination of intense plastic deformation and intense thermal cycling induces dynamic recrystallization in the stir zone, forming an ultrafine-grained, equiaxed structure consistent with the Hall-Fitch relationship. According to the Hall-Fitch relationship, smaller grain size increases resistance to plastic deformation. Among the various compositions, the 60:40 sample exhibits the finest grains, as evidenced by the more uniform particle distribution observed in Figure 6c, indicating higher hardness. Uniformly dispersed nanoparticles not only contribute to grain refinement but also to dislocation strengthening. The hard, tilted  $\text{Si}_3\text{N}_4$  particles strongly hinder dislocation motion, while the BN flakes, while smoother, align along the shear direction, restricting local plastic flow. This strengthening promotes the formation of auroral rings around dislocations, reduces grain boundary migration, and improves overall indentation resistance. Interestingly, despite its higher  $\text{Si}_3\text{N}_4$  content, the 70:30 composition exhibits lower hardness than the 60:40 composite. This suggests that excessive hard particle content may promote cluster formation and weak bond regions, thereby locally reducing the strengthening effect. On the other hand, the 50:50 sample with a higher BN content exhibits a slight increase in hardness, but does not exceed that of the 60:40 ratio, as excess BN weakens the interfacial bonding with the aluminum matrix and reduces load transfer efficiency. Therefore, the optimal mechanical properties do not depend on the absolute presence of  $\text{Si}_3\text{N}_4$ , but rather on a balance between the hardness and lubricity of the reinforcement, which facilitates grain refinement and uniform dispersion.

These results support the observation that the hardness improvement is a result of the combined effects of grain refinement, particle-induced potential resistance, and reinforcement load-bearing contribution. The 60:40  $\text{Si}_3\text{N}_4$ -BN composite, with the finest microstructure and uniform particle distribution, achieves the optimal balance and exhibits the highest hardness among the ratios tested. These trends are consistent with existing studies of metal-ceramic hybrid systems, in which the intermediate reinforcement ratio material exhibits superior mechanical properties to the two extreme reinforcement ratios [32,33]. Therefore, this study demonstrates that FSP hybrid reinforcements provide a viable approach to increasing the hardness of aluminum alloys beyond the limits of single-phase reinforcements.

### 3.6. Tensile properties

The Tensile testing revealed significant differences in the load-bearing capacity of composites with different reinforcement ratios (Figure 10). The ultimate tensile strength (UTS) of the matrix alloy AA5052

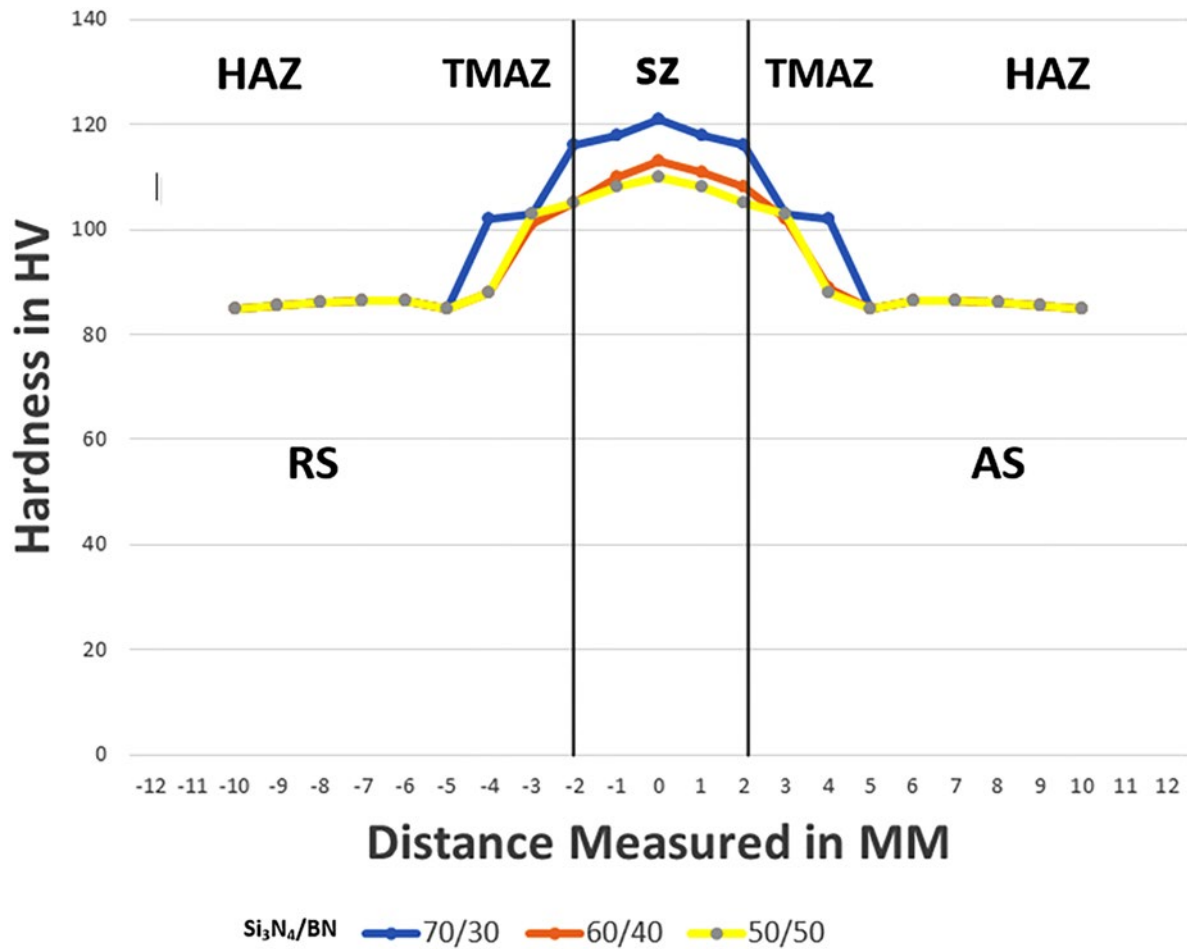


**Figure 9:** Vickers microhardness of AA5052 and hybrid composites with different  $\text{Si}_3\text{N}_4$ -BN ratios.

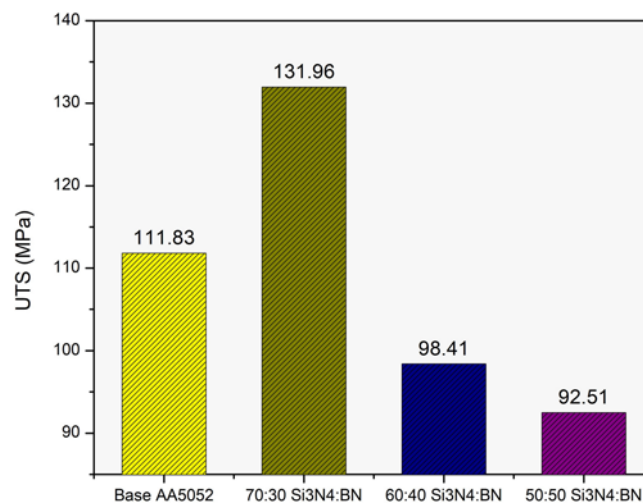


**Figure 10:** Ultimate tensile strengths of AA5052 and hybrid composites with varying  $\text{Si}_3\text{N}_4$ -BN ratios.

was  $111.8 \pm 2.1$  MPa. The 70:30 composite exhibited the highest strength ( $131.9 \pm 2.4$  MPa), an 18% increase over the matrix alloy. This was primarily due to the higher  $\text{Si}_3\text{N}_4$  particle content, which improved load transfer. However, the tensile strength decreased with increasing BN content. The strength of the 60:40 composite was  $98.4 \pm 1.9$  MPa, while that of the 50:50 composite decreased further to  $92.5 \pm 1.7$  MPa. This decrease was

attributed to the relatively weak interfacial bonding between the BN sheets, which facilitated particle detachment under tensile stress. Therefore, while BN improves lubricity and wear resistance, excessive BN reduces strength. These results indicate that  $\text{Si}_3\text{N}_4$  plays a dominant role in tensile reinforcement, while BN primarily contributes to tribological benefits.

### 3.7. Wear behavior

The Dry wear tests showed that all composites exhibited significantly improved wear resistance compared to the unreinforced alloys (Figure 11). The AA5052 matrix exhibited the highest wear rate of  $4.72 \times 10^{-4} \text{mm}^3/\text{N}\cdot\text{m}$ , while all reinforced specimens exhibited significantly reduced wear rates. The 60:40 composite exhibited the best performance, with a wear rate of  $1.99 \times 10^{-4} \text{mm}^3/\text{N}\cdot\text{m}$ , representing a 58% reduction. This improvement is attributed to the synergistic effect of  $\text{Si}_3\text{N}_4$  (which resists abrasive wear) and BN (which acts as a solid lubricant, reducing the friction coefficient to 0.29). The reduced BN fraction in the 70:30 composite reduced lubricity, while the excess BN in the 50:50 composite weakened the particle-matrix interface, facilitating particle extraction. The results showed that the wear rates of both alloys were higher than those of the 60:40 alloy, but still significantly lower than those of the matrix alloy. These results demonstrate that optimizing the mixing ratio is crucial for maximizing tribological performance.

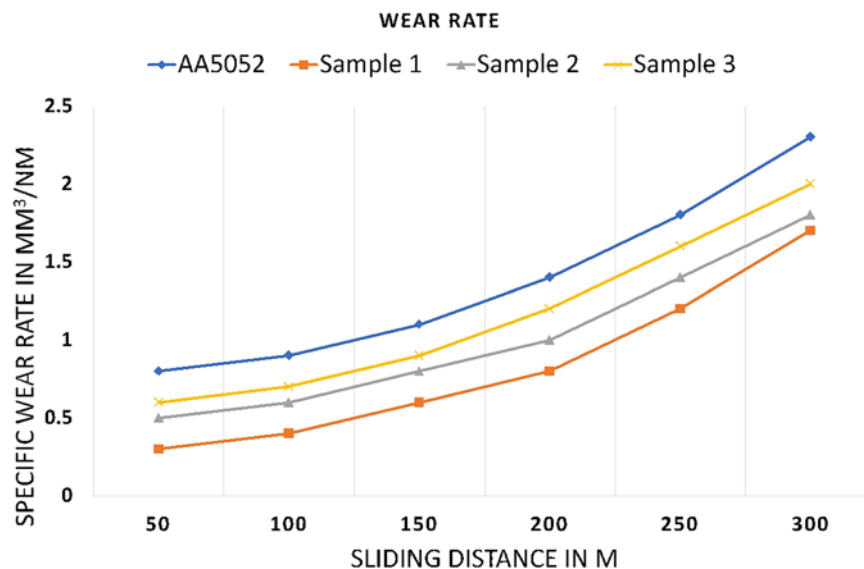


**Figure 11:** Specific wear rates of AA5052 and the hybrid composites (15 N load, 1.2 m/s sliding speed, up to 750 m sliding distance).

### 3.8. Fractography and consolidated analysis

The Fractured specimens subjected to tensile stress were examined using scanning electron microscopy (SEM) to determine the fracture mechanism of each material. The fracture surface of the AA5052-based alloy (Figure 12a) exhibited deep equiaxed pits, indicating a fully ductile fracture mode due to significant plastic deformation. The 70:30  $\text{Si}_3\text{N}_4$ :BN composite (Figure 12b) exhibited a mixed fracture pattern. While pits were still present, they were generally shallower and accompanied by smaller fracture ridges, reflecting the high strength and slightly reduced ductility of this composite. The 60:40 composite (Figure 12c) exhibited primarily shallow fracture feet and brittle fracture zones, indicating that increasing the BN fraction (and thus increasing the matrix stiffness) reduces overall ductility. The fracture surface of the 50:50 composite (Figure 12d) was flat and dominated by brittle features, including clear evidence of wall separation and particle-matrix delamination. These brittle fracture modes are consistent with the significant decrease in tensile strength and elongation. These fracture surface observations confirm that the fracture behavior shifts from ductile to brittle with increasing BN content in the hybrid reinforcement. The results indicate that the 70:30 ratio achieves the optimal balance, exhibiting a blend of ductile and brittle characteristics, equivalent to an intermediate combination of strength and toughness.



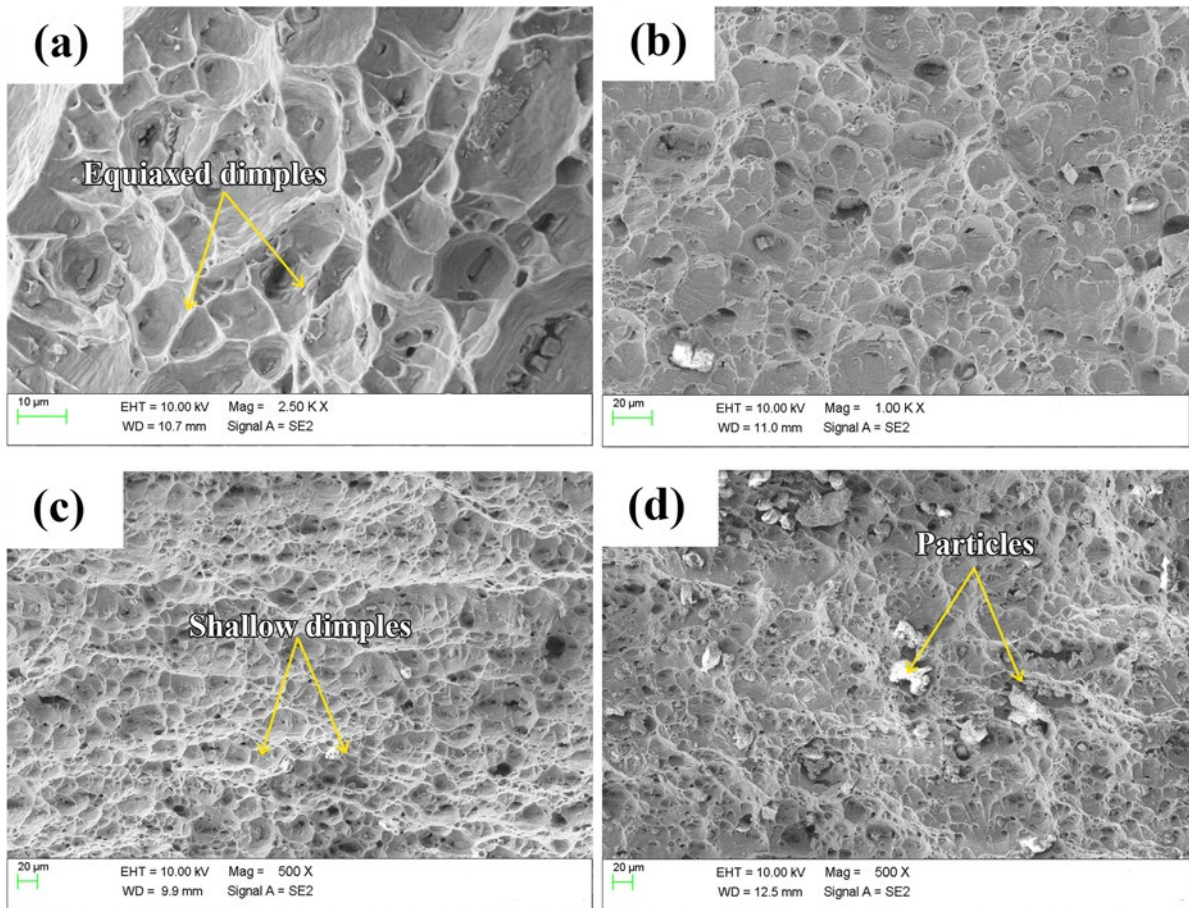


**Figure 12:** Fractography of tensile fracture surfaces: (a) AA5052 base alloy (ductile dimpled rupture); (b) 70:30  $\text{Si}_3\text{N}_4$ :BN composite (mixed ductile–brittle features); (c) 60:40  $\text{Si}_3\text{N}_4$ :BN composite (shallow dimples with some brittle tearing); (d) 50:50  $\text{Si}_3\text{N}_4$ :BN composite (brittle cleavage and particle debonding).

**Table 6:** Summary of key properties for AA5052 and hybrid composites.

MATERIAL	VICKERS HARDNESS (HV)	UTS (MPa)	SPECIFIC WEAR RATE ( $\text{mm}^3/\text{N}\cdot\text{m}$ )
AA5052 (base)	~85	~111.8	$4.72 \times 10^{-4}$
70:30 ( $\text{Si}_3\text{N}_4$ :BN)	~113.6	131.96	↓ vs base (slightly higher than 60:40)
60:40 ( $\text{Si}_3\text{N}_4$ :BN)	~121.1	~98.41	$1.99 \times 10^{-4}$
50:50 ( $\text{Si}_3\text{N}_4$ :BN)	~118.5	~92.51	↓ vs base (higher than 60:40)

To provide a clearer comparison of all reinforcement ratios, the key mechanical and tribological properties are summarized in Table 6. The results confirm that integrating hybrid reinforcements through a multi-pass FSP process significantly alters the properties of AA5052. The 60:40 composite achieves the highest microhardness ( $121.1 \pm 1.2$  HV) and the lowest wear rate ( $1.99 \times 10^{-4} \text{ mm}^3/\text{N}\cdot\text{m}$ ), highlighting the synergistic effect of the hard  $\text{Si}_3\text{N}_4$  particles and the BN lubricating layer. Furthermore, the 70:30 composite exhibits the highest tensile strength ( $131.9 \pm 2.4$  MPa), highlighting the dominant role of  $\text{Si}_3\text{N}_4$  in load-bearing capacity. On the other hand, the 50:50 composite exhibited excellent hardness and low wear, but the high BN content significantly reduced tensile strength and ductility. These results suggest that the hybrid reinforcement ratio plays an important role in balancing hardness, wear resistance, and tensile strength, with composite combinations of 60:40 and 70:30 being the most promising for engineering applications.

#### 4. CONCLUSIONS

We successfully synthesized  $\text{Si}_3\text{N}_4$ -BN hybrid nanoparticle-reinforced AA5052 surface composites using a three-stage friction stir process (FSP). We thoroughly investigated the effects of different reinforcement ratios (70:30, 60:40, and 50:50 wt%) on microstructural evolution, phase stability, hardness, tensile response, wear resistance, and fracture mode. Key findings include:

1. Compared to the cold-rolled AA5052-based alloy, all processed samples achieved significant grain refinement and uniform nanoparticle dispersion. The 60:40  $\text{Si}_3\text{N}_4$ :BN composition exhibited the finest grains and most uniform particle distribution, owing to the effective particle crushing and dynamic recrystallization promoted by the multi-stage stirring.
2. XRD and EDS analyses confirmed the absence of intermetallic compounds such as  $\text{AlN}$  or  $\text{AlB}_2$ , indicating the maintenance of the  $\alpha$ -Al phase as well as the stable  $\text{Si}_3\text{N}_4$  and h-BN phases. This demonstrates good thermal and chemical compatibility between the aluminum matrix and reinforcement during the FSP process.
3. The microhardness values of all composites were significantly higher than those of untreated AA5052. The 60:40 blend ratio achieved the highest hardness (121 HV), attributed to synergistic strengthening mechanisms including Hall-Petch particle refinement, Orowan coverage, and effective load transfer from uniformly dispersed  $\text{Si}_3\text{N}_4$  nanoparticles.
4. The 70:30  $\text{Si}_3\text{N}_4$ :BN composite achieved the highest tensile strength (131.96 MPa), confirming the strength-enhancing effect of  $\text{Si}_3\text{N}_4$ . However, with increasing BN content, the bonding between BN and the Al matrix becomes relatively weak, leading to particle segregation and reduced strength and ductility.
5. Wear resistance of all reinforced composites was significantly improved. The 60:40 composite exhibited the lowest wear-free rate ( $1.99 \times 10^{-4} \text{ mm}^3/\text{N}^4\text{m}$ ) and a low coefficient of friction (0.29).
6. Fractographic analysis revealed that the matrix alloy's fracture mode gradually shifted from ductile to brittle with increasing BN content. The 70:30 composite exhibited a mixed ductile-brittle fracture mode with good particle cohesion, while the 50:50 composite exhibited particle separation and pullout, explaining its poor tensile properties.

Overall, the 60:40  $\text{Si}_3\text{N}_4$ :BN hybrid composite achieved the best balance of hardness, wear resistance, and microstructural homogeneity, while the 70:30 composite exhibited the highest tensile strength. These results demonstrate the potential of FSP-fabricated AA5052 hybrid composites for key applications in aerospace, marine, and automotive sectors, where durability and mechanical properties are paramount. Future research will focus on evaluating the corrosion resistance, high-temperature stability, and long-term fatigue/friction behavior of these hybrid composites in actual use environments to further verify their industrial applicability.

#### 5. BIBLIOGRAPHY

- [1] MIRACLE, D.B., "Metal matrix composites – from science to technological significance", *Composites Science and Technology*, v. 65, n. 15–16, pp. 2526–2540, 2005. doi: <http://doi.org/10.1016/j.compscitech.2005.05.027>.
- [2] HAMPSHIRE, S., "Silicon nitride ceramics: structure and properties", *J Achiev Mater Manuf Eng*, v. 24, n. 1, pp. 43–50, 2007.
- [3] TJONG, S.C., "Novel nanoparticle-reinforced metal matrix composites with enhanced mechanical properties", *Advanced Engineering Materials*, v. 9, n. 8, pp. 639–652, 2007. doi: <http://doi.org/10.1002/adem.200700106>.
- [4] HASHIM, J., LOONEY, L., HASHMI, M.S.J., "Metal-matrix composites: Production by stir casting", *Journal of Materials Processing Technology*, v. 92–93, pp. 1–7, 1999. doi: [http://doi.org/10.1016/S0924-0136\(99\)00118-1](http://doi.org/10.1016/S0924-0136(99)00118-1).
- [5] KAINER, K.U. (ed.), *Metal matrix composites: custom-made materials for automotive and aerospace engineering*. Weinheim, Wiley-VCH, 2006. doi: <http://doi.org/10.1002/3527608117>.
- [6] MAJUMDAR, J.D., MANNA, I., "Laser processing of materials", *Sadhana*, v. 28, n. 3–4, pp. 495–562, 2003. doi: <http://doi.org/10.1007/BF02706446>.
- [7] FAUCHAIS, P., VARDELLE, A., "Thermal sprayed coatings used against corrosion and wear", In: Jazi, H.S. (ed.), *Advanced plasma spray applications*, London, InTech, pp. 3–39, 2012. doi: <http://doi.org/10.5772/34448>

- [8] SURAPPA, M.K., “Aluminum matrix composites: challenges and opportunities”, *Sadhana*, v. 28, n. 1–2, pp. 319–334, 2003. doi: <http://doi.org/10.1007/BF02717141>.
- [9] CLYNE, T.W., WITHERS, P.J. *An Introduction to metal matrix composites*, Cambridge, Cambridge University Press, 1993. doi: <http://doi.org/10.1017/CBO9780511623080>.
- [10] LLOYD, D.J., “Particle reinforced aluminium and magnesium matrix composites”, *International Materials Reviews*, v. 39, n. 1, pp. 1–23, 1994. doi: <http://doi.org/10.1179/imr.1994.39.1.1>.
- [11] PRABU, S.B., KARUNAMOORTHY, L., KATHIRESAN, S., *et al.*, “Influence of stirring speed and stirring time on distribution of particles in cast metal matrix composite”, *Journal of Materials Processing Technology*, v. 171, n. 2, pp. 268–273, 2006. doi: <http://doi.org/10.1016/j.jmatprotec.2005.06.071>.
- [12] ROHATGI, P.K., “Cast aluminum-matrix composites for automotive applications”, *Journal of the Minerals Metals & Materials Society*, v. 43, n. 4, pp. 10–15, 1991. doi: <http://doi.org/10.1007/BF03220538>.
- [13] HAN, N.L., YANG, Z.G., WANG, Z.Q., *et al.*, “Surface composites fabricated by FSP: a review”, *Journal of Materials Science*, v. 49, n. 3, pp. 1058–1073, 2014.
- [14] NABI, N., KHAN, A.A., HUSSAIN, T., *et al.*, “Microstructural and mechanical characterization of NiTi-reinforced AA5052 surface composites fabricated via friction stir processing”, *Journal of Materials Research and Technology*, v. 18, pp. 3640–3652, 2022.
- [15] QU, X., LIU, J., ZENG, Z., *et al.*, “Effect of groove geometry on the distribution and performance of ceramic particles in FSP-processed AA6061 composites”, *Materials Characterization*, v. 180, pp. 111421, 2021.
- [16] MEHTA, K., VISHVESH, D., “Influence of blind-hole filling pattern on wear resistance of B<sub>4</sub>C-reinforced AA6061 composites via friction stir processing”, *Materials Today: Proceedings*, v. 33, pp. 2137–2142, 2020.
- [17] VIGNESH, S., KUMAR, V.R.S., GOPAL, S., “Optimization of friction stir processing parameters for grain refinement and phase dissolution in AA6061–TiB<sub>2</sub> surface composites”, *Materials and Manufacturing Processes*, v. 36, n. 4, pp. 434–442, 2021.
- [18] YADAV, R., CHAUHAN, N., SINGH, P., “Interfacial bonding and mechanical performance of Al–SiC composites produced by FSP: A review and experimental study”, *Journal of Alloys and Compounds*, v. 902, pp. 163633, 2022.
- [19] GIRISH, M., ANANDAKRISHNAN, V., “Optimization of dry sliding wear parameters of FSP-treated AA7075 composites using Taguchi method”, *Tribology in Industry*, v. 42, n. 1, pp. 35–46, 2020.
- [20] PATEL, K., RANA, R., YADAV, V., “Fabrication and characterization of AZ31/ZrO<sub>2</sub> nanocomposites using FSP for wear and hardness enhancement”, *Materials Research Express*, v. 8, n. 8, pp. 085005, 2021.
- [21] MISHRA, R.S., MA, Z.Y., “Friction stir welding and processing”, *Materials Science and Engineering R Reports*, v. 50, n. 1–2, pp. 1–78, 2005. doi: <http://doi.org/10.1016/j.mser.2005.07.001>.
- [22] RILEY, F.L., “Silicon nitride and related materials”, *Journal of the American Ceramic Society*, v. 83, n. 2, pp. 245–265, 2000. doi: <http://doi.org/10.1111/j.1151-2916.2000.tb01182.x>.
- [23] KLEMM, H., “Silicon nitride for high-temperature applications”, *Journal of the American Ceramic Society*, v. 93, n. 6, pp. 1501–1522, 2010. doi: <http://doi.org/10.1111/j.1551-2916.2010.03839.x>.
- [24] PAWLAK, Z., KALDONSKI, T., PAI, R., *et al.*, “Tribological properties of boron nitride”, *J Achiev Mater Manuf Eng*, v. 37, n. 2, pp. 498–504, 2009.
- [25] EICHLER, J., LESNIAK, C., “Boron nitride composites in high-temperature applications”, *Journal of the European Ceramic Society*, v. 28, n. 5, pp. 1105–1109, 2008. doi: <http://doi.org/10.1016/j.jeurceramsoc.2007.09.005>.
- [26] YAMADA, K., OKAMOTO, N., MURAKAMI, Y., *et al.*, “Tribology of boron nitride”, *Wear*, v. 254, n. 5–6, pp. 417–425, 2003.
- [27] KUMAR, N., GAUTAM, R.K., MOHAN, S., “Tribological behavior of hybrid metal matrix composite”, *International Journal of Engineering Science and Technology*, v. 10, n. 2, pp. 135–147, 2018.
- [28] ZHAO, Q., ZHANG, D., QIU, F., “Laser cladding of hybrid composites”, *Surface and Coatings Technology*, v. 206, n. 22, pp. 4647–4652, 2012.
- [29] SINGH, J., CHAUHAN, A., KUMAR, S., “Optimization of hybrid composites”, *Materials Science Forum*, v. 775–776, pp. 11–17, 2014. doi: <http://doi.org/10.4028/www.scientific.net/MSF.775-776.11>.



- [30] WANG, J., YANG, Q., MA, P., “Effect of particle dispersion in metal matrix composites”, *Compos Part A*, v. 89, pp. 128–138, 2016.
- [31] MEHDI, H., BATRA, L., SINGH, A.P., *et al.*, “Multi-response optimization of FSW process parameters of dissimilar aluminum alloys of AA2014 and AA6061 by response surface methodology (RSM)”, *Int J Interact Des Manuf*, v. 18, n. 3, pp. 1507–1522, 2024. doi: <http://doi.org/10.1007/s12008-023-01409-2>.
- [32] RANI, P., MISRA, R.S., MEHDI, H., “Effect of nano-Sized Al<sub>2</sub>O<sub>3</sub> Particles on Microstructure and Mechanical Properties of Aluminum Matrix Composite Fabricated by Multipass FSW”, *Proceedings of the Institution of Mechanical Engineers. Part C, Journal of Mechanical Engineering Science*, v. 0, n. 0, pp. 09544062221110822, 2022. doi: <http://doi.org/10.1177/09544062221110822>.
- [33] MEHDI, H., MISHRA, R.S., “Consequence of reinforced SiC particles on microstructural and mechanical properties of AA6061 surface composites by multi-pass FSP”, *Journal of Adhesion Science and Technology*, v. 36, n. 12, pp. 1279–1298, 2021. doi: <http://doi.org/10.1080/01694243.2021.1964846>.
- [34] MEHDI, H., MISHRA, R.S., “Effect of multi-pass friction stir processing and SiC nanoparticles on microstructure and mechanical properties of AA6082-T6”, *Advances in Industrial and Manufacturing Engineering*, v. 3, pp. 100062, 2021. doi: <http://doi.org/10.1016/j.aime.2021.100062>.